Physica B 715 (2025) 417615

Contents lists available at ScienceDirect

Physica B: Condensed Matter

journal homepage: www.elsevier.com/locate/physb

Computational investigation of structural, electronic, and optical properties of $(In_xGa_{1-x})_2O_3$ alloys as candidates for emitter layer application in solar cells

B. K C [a], V.T. Barone [a], S.R. Kandel [a], M. Sitaula [a], B.B. Dumre [b], R.J. Ellingson [a], S.V. Khare [a,*]

[a] Department of Physics and Astronomy, and Wright Center for Photovoltaics Innovation and Commercialization (PVIC), University of Toledo, Toledo, OH, 43606, USA
[b] University of California, Merced, CA, 95343, USA

ARTICLE INFO

Keywords:
$(In_xGa_{1-x})_2O_3$
Density functional theory
First-principles calculation
Electronic properties
Vibrational properties
Optical properties

ABSTRACT

Indium gallium oxide has recently been widely investigated experimentally for applications such as solar cells and other applications. In this study, we computationally investigate $(In_xGa_{1-x})_2O_3$ alloy system (x = 0.00, 0.25, 0.50, 0.75, 1.00) in the trigonal crystal structure in R $\bar{3}$ c space group for photovoltaic application using density functional theory (DFT) and beyond methods. The lattice constants and bandgap values (4.4–2.6 eV) for end members align closely with both experimental and computational studies. Mechanical and vibrational analyses reveal that all the alloys are mechanically and dynamically stable. The Crystal Orbital Hamilton Population (COHP) analysis shows predominantly positive bonding states below the Fermi level. All the alloys display significantly higher average hole-effective masses compared to electron-effective masses. Optical property analysis shows lower absorption coefficient and reflectivity, suggesting $(In_xGa_{1-x})_2O_3$ alloys as candidates for emitter layer material in solar cells.

1. Introduction

Research on new materials has been actively pursued to enhance the efficiency of solar cells by optimizing their various layers. CdTe-based solar cells have shown the potential to achieve efficiency of up to 28 % [1,2]. Transparent conducting oxide (TCO) layers play a crucial role in improving the performance and efficiency of solar cells. TCO materials, such as magnesium oxide (MgO) and zinc oxide (ZnO), are mostly used in this layer [3]. In recent years, indium oxide (In_2O_3), known for its optical transparency having n-type conductivity [4,5] and gallium oxide (Ga_2O_3), with their favorable electronic and optical properties, are widely used as a strong candidate for use in the TCO layer [6,7]. Dive et al. suggested that In_2O_3 and Ga_2O_3 alloys, with tunable bandgaps ranging from 2.6 to 4.8 eV, can be used as a TCO and emitter layer in CdTe-based solar cells with an efficiency of 17.59 % [8].

Several experimental studies have explored In_2O_3, Ga_2O_3, and the $(In_xGa_{1-x})_2O_3$ alloy system across various crystal structures. Swallow et al. studied the $(In_xGa_{1-x})_2O_3$ alloy system ($0.01 \leq x \leq 0.82$) computationally using density functional theory (DFT) with Heyd-Scuseria-Ernzerhof hybrid functional (HSE06) and experimentally through pulsed laser deposition (PLD). The study examined the monoclinic, hexagonal, and bixbyite phases, highlighting their potential as transport conductors and photodetectors [9]. Experimental study on the orthorhombic structure with indium [In] ranging from 0 to 0.38 displayed the bandgap values of ~4.1–4.9 eV, obtained using PLD [10,11]. Kokubun et al. investigated the $(In_xGa_{1-x})_2O_3$ alloy system ($0 \leq x \leq 0.3$) in the monoclinic phase, prepared using the sol-gel method, and reported a linear decrease in bandgap from 5.0 to 4.2 eV [12]. Similarly, Jamarkattel et al. studied $(In_xGa_{1-x})_2O_3$ alloy system, highlighting its potential as an emitter layer in CdTe solar cells with an efficiency of 16 % at x = 0.36 and a bandgap of 4.03 eV. This study was performed using spectroscopic ellipsometry and characterized the alloy system as amorphous [13,14].

Earlier computational studies have examined the $(In_xGa_{1-x})_2O_3$ alloy system for various structures, focusing on their different properties. Peelaers et al. studied the structural and electronic properties of both monoclinic and cubic structures using DFT for [In] up to 50 % [15]. Similarly, Liu et al. examined the electronic properties of the

* Corresponding author.
E-mail address: sanjay.khare@utoledo.edu (S.V. Khare).

https://doi.org/10.1016/j.physb.2025.417615
Received 13 April 2025; Received in revised form 5 July 2025; Accepted 15 July 2025
Available online 18 July 2025

$(In_xGa_{1-x})_2O_3$ alloy system in the monoclinic crystal structure. The bandgap values in this work were reported to decrease from 4.81 to 4.42 eV when [In] increased up to 18.75 %, thereby highlighting the material's potential for UV photodetectors [16]. The end members, In_2O_3 and Ga_2O_3, have also been studied computationally and experimentally. He et al. reported the structural, electronic, and optical properties of Ga_2O_3 in monoclinic and hexagonal structures using DFT [17]. Grundmann et al. examined the elastic properties of Ga_2O_3 in monoclinic and trigonal phases, supporting its applications in thin films [18]. Additionally, Ga_2O_3 has been studied in detail, using DFT with GGA + U, reporting its structural, electronic, and optical properties across trigonal, monoclinic, orthorhombic, and cubic phases. In this work, lattice parameters, bandgaps, and electron effective masses have been well-documented for all these structures [19]. For In_2O_3, DFT studies have reported the optical and electronic properties of the cubic, orthorhombic, and trigonal crystal structures [20,21]. Boer et al. reported the bandgap value for trigonal crystal structure in R $\overline{3}$ c space group to be 1.30 eV using DFT with PBE-GGA [22]. However, a detailed computational study on R $\overline{3}$ c space group for the $(In_xGa_{1-x})_2O_3$ alloy system is still lacking, leaving significant gaps in understanding their properties.

Hence, in this work, we computed the structural, energetic, elastic, mechanical, electronic, and optical properties of $(In_xGa_{1-x})_2O_3$ ($0 \leq x \leq 1$) alloy system in the trigonal crystal structure in R $\overline{3}$ c space group using DFT and beyond. The calculated lattice constants for the end members showed good agreement with experimental and computational results. With the increase in [In], a linear decrease in the formation energy and the bandgap values were observed. The average electron effective masses were much lower than the hole effective masses for all the alloys. The HSE06 functional was employed to obtain electronic and optical properties. COHP analysis provided insights into the bonding and antibonding interactions. Phonon calculations indicated that all the alloys are dynamically stable. Additionally, analysis of absorption coefficient and reflectivity suggests that $(In_xGa_{1-x})_2O_3$ alloy system can be used as an emitter layer in solar cells.

2. Computational methods

All DFT calculations were performed using the Vienna Ab initio Simulation Package (VASP) [23–25]. The Perdew-Burke-Ernzerhof (PBE) [26] Generalized Gradient Approximation (GGA) exchange-correlation functional was used within Projector-Augmented-Wave (PAW) method [24,27,28]. Ga_d, In_d, and O pseudopotentials were used from the VASP library. The computations were performed on k-point meshes of size (6 × 6 × 2) with the plane wave cutoff energy set at 500 eV [29]. Gaussian smearing of width 0.05 eV [30,31] was used to set the partial occupancies. The electronic convergence criteria were set to an energy tolerance of 10^{-6} eV. The structural convergence criteria were set to a force tolerance of 0.01 eV/Å. For the end members, the crystal structure of the materials was obtained from the Materials Project [32]. Special Quasirandom Structures (SQS) [33] were generated using mcsqs code within Alloy Theoretical Automated Toolkit (ATAT) [34] to calculate the random Ga/In occupation in the crystal structures for x = 0.25, 0.50, and 0.75. To ensure the reliability of the SQS-generated structures, three different atomic configurations for each composition (x = 0.25, 0.50, and 0.75) were used to calculate the lattice constants and bandgaps. The maximum deviations observed were below 0.03 Å for lattice constants and 0.04 eV in HSE06 bandgaps across the structures. These minimal deviations suggest that a single representative structure is sufficient to capture the alloy behavior precisely. The structures employed in our computational investigations are presented in Table S5.

Atomic positions, cell shape, and cell volume were relaxed while optimizing the geometry of the crystal structures. Following relaxation, the calculation of formation energy per formula unit of $(In_xGa_{1-x})_2O_3$ was calculated as [35–37]:

$$E_{form} = E[(In_xGa_{1-x})_2O_3] - 2[xE(In) + (1-x)E(Ga)] - 3E(O_2)\,/\,2, \quad (1)$$

where E(In), E(Ga), and $E(O_2)$ are the ground state energies of indium (space group: I4/mmm), gallium (space group: Cmce), and oxygen dimers in vacuo, respectively.

Next, the elastic constants were calculated by computing the Hessian matrices of directional second derivatives of energy with respect to cell distortions using finite differences. The elastic moduli were determined using the equation that involves the components of stiffness (C_{ij}) and compliance (S_{ij}) tensors following the Voigt-Reuss-Hill approximation [38–43] equations. The following equations provide bulk modulus (B) and shear modulus (G):

$$B_V = [C_{11} + C_{22} + C_{33} + 2(C_{12} + C_{23} + C_{31})]\,/\,9 \quad (2)$$

$$G_V = [C_{11} + C_{22} + C_{33} - C_{12} - C_{23} - C_{31}) + 3(C_{44} + C_{55} + C_{66})]\,/\,15 \quad (3)$$

$$B_R = [S_{11} + S_{22} + S_{33} + 2(S_{12} + S_{23} + S_{31})]^{-1} \quad (4)$$

$$G_R = 15[4(S_{11} + S_{22} + S_{33} - S_{12} - S_{23} - S_{31}) + 3(S_{44} + S_{55} + S_{66})]^{-1} \quad (5)$$

The following equations provide average bulk and shear modulus [44]:

$$B = (B_V + B_R)\,/\,2 \text{ and } G = (G_V + G_R)\,/\,2. \quad (6)$$

Thus, the values of B and G were used to calculate Pugh's ratio ($k = G/B$) and Vickers hardness (Hv) using the equation recommended by Tian et al. [45–47] as:

$$H_V = 0.92k^{1.137}G^{0.708} \quad (7)$$

Furthermore, we calculate the Poisson's ratio (v) and Young's modulus (Y) using the values B and G as:

$$v = (3-2k)/(6+2k),\ Y = 9G/(3+k) \quad (8)$$

Additionally, Born stability criteria [48] were used to test the mechanical stability of each composition given by.

$$C_{11} > |C_{12}|,\ 2C_{13}^2 < C_{33}\,(C_{11} + C_{12}),\ C_{44} > 0, \text{and } C_{66} > 0 \quad (9)$$

Band structure, Crystal Orbital Hamilton Population (COHP), and effective masses calculations were performed using GGA functional. GGA and the Local Density Approximation (LDA) exchange-correlation functionals underestimate the electronic bandgaps [49]. Hence, in these calculations, HSE06 functional with 25 % of the exact exchange from the Hartree-Fock theory, and 75 % of the exchange from GGA is implemented [50,51]. This functional has predicted the experimental bandgaps more precisely for semiconductors and insulators [46,52]. Therefore, the hybrid HSEO6 functional was employed to calculate the electronic density of states (DOS) and optical properties. Electronic bandgaps were calculated using both GGA and HSE06 functional. The Sumo package [53] was used to calculate the effective masses of holes (m_h^*) and electrons (m_e^*) from the computed band structures.

The Phonopy [54] software package was deployed to study the dynamical stability of $(In_xGa_{1-x})_2O_3$. The structure is stable if there is no imaginary phonon frequency; otherwise, it is dynamically unstable. We further analyzed the chemical bonding. The COHP analysis was done using the Local Orbital Basis Suite Towards Electronic-Structure Reconstruction (LOBSTER) [55–60]) program using the default basis function: Ga (3d 4s 4p), In (4d 5s 5p) and O (2s 2p). Furthermore, we used the Bader analysis [61–64] to calculate the effective charge transfer.

3. Results

3.1. Structural parameters

Both the end members (R $\bar{3}$ c) and the intermediate members (P3) with trigonal space group contain 20 atoms, modeled using SQS [33] approach. In the $(In_xGa_{1-x})_2O_3$ alloys, the cations and anions are positioned at the 12c and 18e Wyckoff positions. Table 1 presents the computed lattice parameters, indicating that these values increase with higher x values in $(In_xGa_{1-x})_2O_3$, directly related to ionic radius following Vegard's law [65]. The results are consistent with the previous computational results for the end members, calculated using DFT [20, 66,67]. However, a 1.5–4.5 % deviation from the experimental results [22,68,69] is attributed to the use of the GGA [26]. Table S1 details the average bond lengths of the first nearest neighbors. In Ga_2O_3, the bond length between Ga-O is approximately 1.90 Å, while the bond length for In-O in In_2O_3 is around 2.20 Å.

The formation energy calculated using Equation (1) is presented in Table 1. The energy values change from −10.80 eV for each Ga_2O_3 molecule to −9.53 eV for In_2O_3, following a linear trend as the composition changes from ($0 \leq x \leq 1$). This trend shows that increasing [In] in $(In_xGa_{1-x})_2O_3$ gradually decreases stability. Fig. S2 presents the X-ray diffraction (XRD) results for all values of x, generated using VESTA [70]. For pure Ga_2O_3, a slight deviation of 2° is observed at the 2θ value of 32° compared to the experimental peaks [71]. Similarly, for In_2O_3, the deviation is by a small margin of 1° at 31° [72]. Increasing the value of x from 0 to 1 for the alloy system consistently shifts the peak to the left, corresponding with increasing lattice parameters. Our XRD figure for the intermediate compositions is predictive, as no experimental data is available.

3.2. Mechanical properties

The fully relaxed structures were used to calculate the elastic and mechanical properties. The elastic stiffness constants (C_{ij}) were obtained using VASP with the GGA functional, and the compliance tensors (S_{ij}) were derived by taking the inverse of (C_{ij}). Equations (2)–(8) were employed to predict bulk modulus (B), shear modulus (G), Vickers hardness (H_V), Pugh's ratio (k), and Young's modulus (Y), as presented in Table 2. The calculated elastic constants were further used to evaluate the mechanical stability of all compounds in the $(In_xGa_{1-x})_2O_3$ alloys. Each component of the alloy satisfies the Born stability criteria [73] as presented in equation (9), confirming their mechanical stability.

The calculated values of bulk moduli range from 216 GPa to 163 GPa, while shear moduli range from 100 GPa to 67 GPa. As the [In] increases in $(In_xGa_{1-x})_2O_3$, both bulk and shear moduli decrease, which may be attributed to the mechanical softening, consistent with the findings reported by Liu et al. [74]. The Pugh's ratio varies between 0.41 (x = 1.00) and 0.59 (x = 0.25). According to Pugh's criteria, materials with $k = G/B < 0.57$ are considered ductile, while those with higher values are classified as brittle [75]. Therefore, all compositions in this study exhibit ductile behavior except x = 0.25, which falls in the brittle regime. The Vickers hardness of CdTe, a widely used solar cell material, is 0.49 GPa [76]. In contrast, the $(In_xGa_{1-x})_2O_3$ alloy system exhibits significantly higher hardness values, ranging from 6.66 to 12.10 GPa. These enhanced hardness values compared to CdTe suggest that all members of the alloy system are suitable for use in solar cell applications.

Table 1
Lattice vector lengths and formation energy per formula unit of $(In_xGa_{1-x})_2O_3$ computed using GGA functional.

Material	Space Group	a (Å)	c (Å)	c/a	Formation Energy (eV)
Ga_2O_3	R $\bar{3}$ c	5.05, 5.05[a], 4.98[b]	13.61, 13.61[a], 13.43[b]	2.69	−10.80
$(In_{0.25}Ga_{0.75})_2O_3$	P3	5.18	13.84	2.67	−10.34
$(In_{0.50}Ga_{0.50})_2O_3$	P3	5.29	14.11	2.67	−9.99
$(In_{0.75}Ga_{0.25})_2O_3$	P3	5.41	14.30	2.65	−9.66
In_2O_3	R $\bar{3}$ c	5.57, 5.49[c], 5.48[d], 5.48[e]	14.72, 14.42[c], 14.49[d], 14.51[e]	2.64	−9.53

[a] Theoretical Ref. [66].
[b] Experimental Ref. [68].
[c] Theoretical Ref. [20].
[d] Experimental Ref. [22].
[e] Experimental Ref. [69].

Table 2
Bulk modulus (B), shear modulus (G), Young's modulus (Y), Vickers hardness (H_V), Pugh's ratio (k), and Poisson's ratio (v) for $(In_xGa_{1-x})_2O_3$ alloys.

Material	B (GPa)	G (GPa)	Y (GPa)	H_V (GPa)	k	v
Ga_2O_3	216.33	100.63	261.76	10.08	0.46	0.30
$(In_{0.25}Ga_{0.75})_2O_3$	144.61	86.68	217.30	12.10	0.59	0.25
$(In_{0.50}Ga_{0.50})_2O_3$	179.20	79.10	206.91	8.00	0.44	0.31
$(In_{0.75}Ga_{0.25})_2O_3$	169.95	77.12	200.98	8.12	0.45	0.30
In_2O_3	163.19	67.59	178.17	6.66	0.41	0.31

3.3. Electronic properties

3.3.1. Density of states

Fig. 1 displays the local density of states (LDOS) for varying x in $(In_xGa_{1-x})_2O_3$, computed using the hybrid HSE06 functional. The figure demonstrates the changes in electronic structure with increasing [In]. LDOS analysis reveals that O states dominate both below and above the Fermi level across all the compositions. For pure Ga_2O_3 (x = 0), the LDOS is influenced by O and Ga. As [In] is introduced, the Ga contributions are progressively surpassed by In, highlighting the impact of In on the electronic properties. Above the Fermi level, states begin to appear after the bandgap for all the compositions, confirming their non-metallic nature and indicating that the alloys exhibit semiconducting

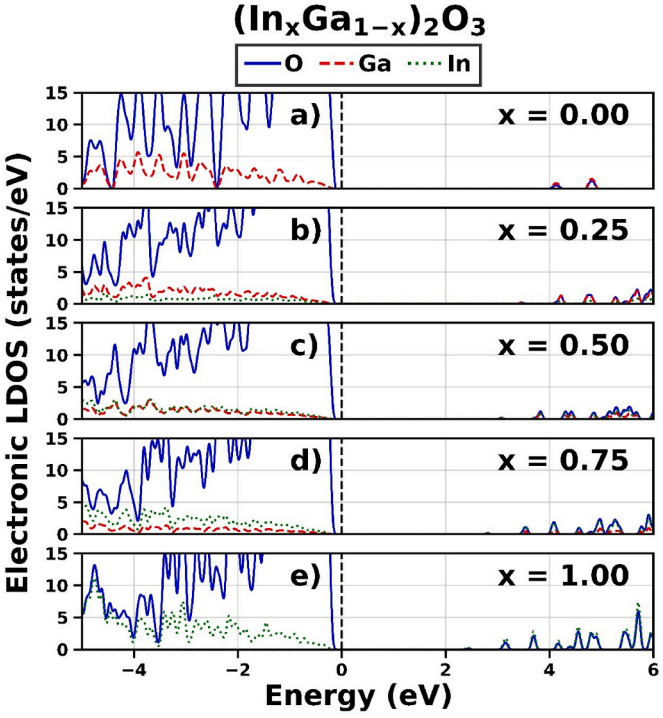

Fig. 1. Electronic Local density of states (LDOS) for $(In_xGa_{1-x})_2O_3$ alloys calculated using HSE06 functional. The Fermi energy is set at 0 eV.

behavior.

As in Fig. 3, our bandgap calculations for the $(In_xGa_{1-x})_2O_3$ alloy system show a composition-dependent bowing behavior. The bowing parameter, $\delta_p = 0.86$ eV, was obtained using the standard bandgap bowing formula.

$$p(x) = xp(1) + (1-x)p(0) - x(1-x)\delta_p, \quad (10)$$

where x is the [In] in the alloy, while $p(x)$ are the HSE06 functional bandgaps for $(In_xGa_{1-x})_2O_3$. Our bandgap calculations show a linear trend with increasing [In], ranging from 4.4 eV to 2.6 eV. Kawamura et al. reported a bandgap of 4.68 eV for Ga_2O_3, calculated using Quantum Espresso with the hybrid HSE03 functional [77], while the bandgap value for pure In_2O_3 was reported as 2.44 eV using DFT with hybrid HSE03 functional [67]. These previously reported computational results show strong agreement with our calculated values, as presented in Table 3. Furthermore, experimental results obtained from PLD, X-ray absorption, and emission spectroscopy show an approximate deviation of less than 16 % from our calculated bandgaps [22,78–80].

3.3.2. Charge transfer

Charge transfer for all the alloys of $(In_xGa_{1-x})_2O_3$ was calculated using the Bader charge analysis. This represents the amount of negative charge in terms of elementary electronic charge (-e) transferred from Ga-O and In-O. The average charge transfer values are presented in Table S3. The charge transfer from Ga to O ranges from 1.88 e in pure Ga_2O_3 to 1.84 e in $(In_{0.75}Ga_{0.25})_2O_3$. Meanwhile, the charge transfer from In to O remains consistent at 1.85 e across all the alloys, except for pure In_2O_3, which decreases to 1.82 e. This value for pure In_2O_3 aligns well with the findings of Karazhanov et al., who reported a charge transfer of 1.82 e using a similar approach [20]. As the charge transferred is greater than 1 e, the bonds are ionic in nature [52]. Based on the electrostatic force calculated by Allred et al. [81] the electronegativities of Ga, In, and O are 1.82 e, 1.49 e, and 3.50 e, respectively. The electronegativity difference in In-O bonds (2.01 e) is higher than in Ga-O bonds (1.68 e). However, we observe that Ga-O bonds exhibit a higher charge transfer value compared to In-O bonds. Hence, we suspect that the higher charge transfer from Ga-O bonds may be due to its shorter bond lengths or orbital interactions, which aligns with similar observations reported by Dumre et al. [82].

3.3.3. Crystal orbital Hamilton population

The negative projected crystal orbital Hamilton population (-pCOHP) calculations for all the alloy compositions were performed to analyze the bonding and antibonding behavior using the GGA functional as presented in Fig. 2. The -pCOHP analysis above the baseline indicates positive bonding, whereas below the baseline corresponds to antibonding interactions. The baseline itself represents no net bonding. The study was performed between 1.8 and 2.3 Å for the first nearest

Table 3
Electronic bandgap of $(In_xGa_{1-x})_2O_3$ computed using GGA and hybrid HSE06 functional.

Material	Band gap (eV)	
	GGA	HSE06
Ga_2O_3	2.41	4.40, 4.68[a], 4.90[b], 5.30[c]
$(In_{0.25}Ga_{0.75})_2O_3$	1.88	3.70
$(In_{0.50}Ga_{0.50})_2O_3$	1.56	3.29
$(In_{0.75}Ga_{0.25})_2O_3$	1.31	3.02
In_2O_3	0.98	2.63, 2.44[c], 3.10[d], 3.0[e]

[a] Theoretical Ref. [77].
[b] Experimental Ref. [78].
[c] Experimental Ref. [79].
[d] Theoretical Ref. [67].
[e] Experimental Ref. [22].
[f] Experimental Ref. [80].

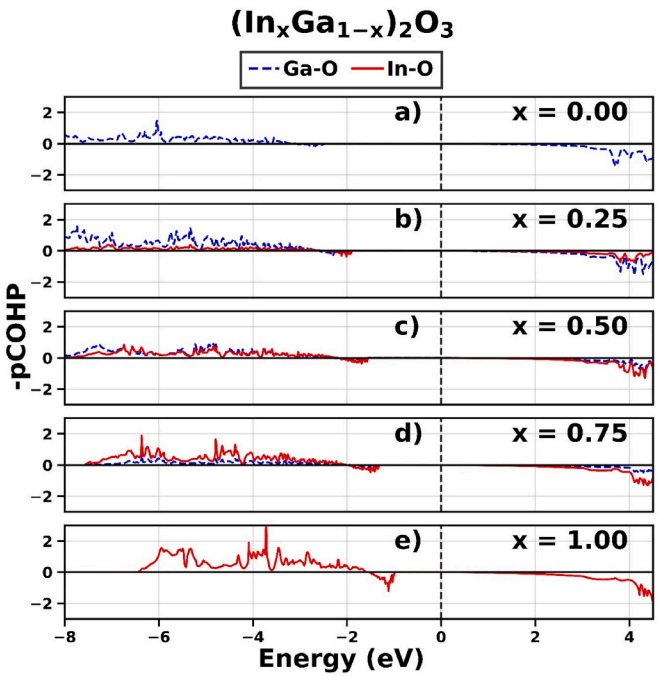

Fig. 2. Negative Projected Crystal Orbital Hamilton Population (-pCOHP) interaction of Ga-O and In-O in $(In_xGa_{1-x})_2O_3$ for the 1st nearest neighbor interaction. The positive and negative values of -pCOHP represent the bonding and antibonding interactions respectively. The Fermi energy is set at 0 eV.

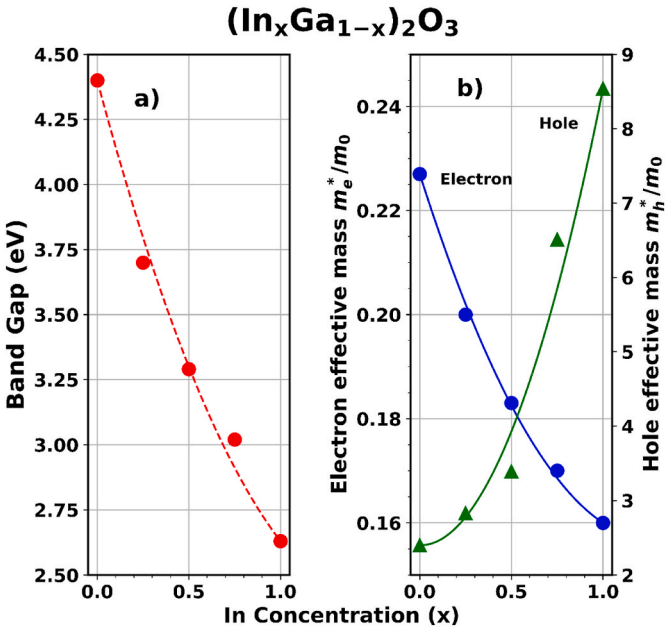

Fig. 3. a) Electronic bandgap calculated using HSE06 functional and b) Electron effective masses (m^*_e) and hole effective masses (m^*_h) of $(In_xGa_{1-x})_2O_3$ alloys. Here, the points represent calculated data, whereas the curves are fitted using sketching parameters as defined in Eq. (10).

neighbors of (Ga-O) and (In-O). For x = 0, 0.25, and 0.50, almost all the population has positive bonding below the Fermi level. As [In] increases, a downward peak shows antibonding. The integrated total COHP (iCOHP) is also calculated to provide further information on the total bond strength. For pure Ga_2O_3 (x = 0), iCOHP is −3.88 eV. With the increase in [In], iCOHP becomes less negative and is −3.14 eV for pure In_2O_3 (x = 1). The formation energy calculation in Table 1 shows a

similar trend, with the energy values becoming less negative as [In] is added. Therefore, both the formation energy and the iCOHP show a trend where increasing [In] leads to the reduced stability of the material.

3.3.4. Effective masses

Table S4 presents the average effective masses for all the compositions of $(In_xGa_{1-x})_2O_3$ calculated using GGA functional. As [In] increases, the electron effective masses (m_e^*) decrease from 0.27 to 0.16, while the hole effective masses (m_h^*) increase from 2.40 to 8.50. For pure Ga_2O_3, the computational results for m_e^*, with GGA + U have been reported as 0.30 and 0.28 [19,83] and 0.16 with LDA for In_2O_3 [20]. The electron effective mass for x = 0 and x = 1 is observed along Γ to L, Z, and X directions, while for x = 0.25, x = 0.50, and x = 0.75, it is observed along the Γ to M, K, and A directions. In all the crystal structures, m_h^* is higher than m_e^*, suggesting that electrons are expected to move freely as the majority charge carriers.

To visualize the deviation from linearity in the physical quantity $(p(x))$, we used the bowing expression as described in Equation (10), where x is the [In] in the alloy, while $p(1)$ and $p(0)$ are the effective masses for pure In_2O_3 and Ga_2O_3, respectively. The bowing parameters are 0.043 for m_e^* and 6.17 for m_h^*.

The charge carrier mobility values of the $(In_xGa_{1-x})_2O_3$ alloy system are summarized in Table S4. We calculated the carrier transport characteristics using the relation $\mu = e\tau/m^*$ [84]. In our study, the electron mobilities range from 76.37 cm^2/Vs to 110.34 cm^2/Vs within the alloy system. As a benchmark, materials commonly employed in TCO and emitter layers of solar cells have electron mobilities greater than 65 cm^2/Vs [85,86]. These results, together with a low absorption coefficient (α) as shown in Fig. 5, suggest that the $(In_xGa_{1-x})_2O_3$ alloy system possesses both the required transport and optical properties, making it a suitable candidate for use in emitter layer applications in solar cells.

3.4. Vibrational properties

As shown in Fig. 4, the phonon LDOS for all the compositions of

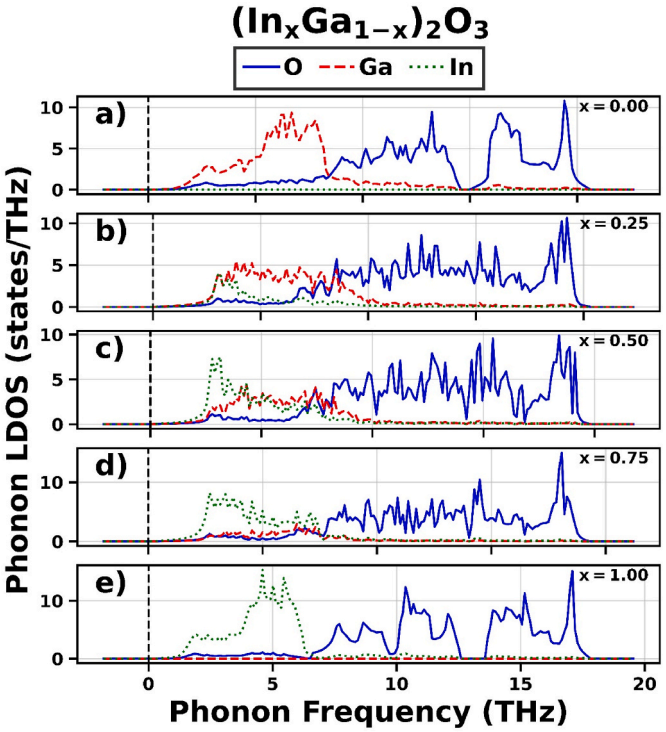

Fig. 4. Phonon local densities of states (LDOS) of $(In_xGa_{1-x})_2O_3$ computed using GGA functional.

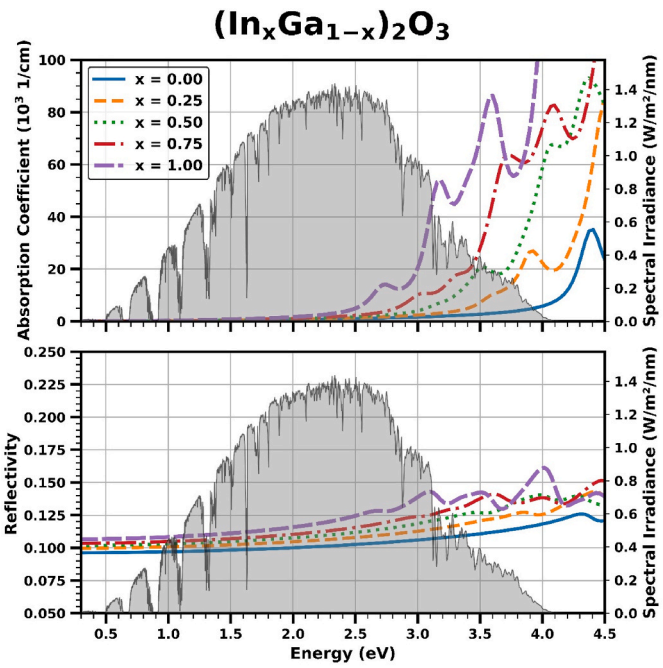

Fig. 5. Absorption coefficient and reflectivity curves of $(In_xGa_{1-x})_2O_3$ alloys using hybrid HSE06 functional. The shaded region represents the AM 1.5 G solar spectrum irradiance [88].

$(In_xGa_{1-x})_2O_3$ were computed using the GGA functional. These calculations confirm that all the alloys are dynamically stable, with no phonon LDOS in the imaginary phonon frequency region. The phonon LDOS reveals that O atoms vibrate at higher frequencies at around 17 THz, followed by Ga at 6 THz and In at 4 THz. This trend indicates that lighter atoms vibrate at higher frequencies than heavier atoms. Furthermore, small phonon LDOS bandgaps, between 13 THz and 14 THz, are observed for the end members, qualifying them as potential candidates for sound filtering and mirror applications, as any phonon of frequencies within the gap will not penetrate the material and will be reflected from the surface [87]. In contrast, the intermediate alloy compositions lack phonon LDOS bandgaps, disqualifying them for such applications.

3.5. Optical properties

The optical properties for all five members of the $(In_xGa_{1-x})_2O_3$ alloy system were calculated using hybrid HSE06 functional. The absorption coefficient (α) and reflectivity (R) are plotted against photon energy, as shown in Fig. 5. The absorption coefficient ranges from 10^3 cm^{-1} to 10^5 cm^{-1} until $\hbar\omega = 4.5$ eV. Below $\hbar\omega = 2.5$ eV, there is no significant rise in α for any alloys within the visible region. However, a noticeable rise is observed as the photon energy exceeds 2.5 eV. For x = 0, the (α) peak occurs at $\hbar\omega = 4.4$ eV. With the increase in [In], the peak shifts to lower photon energy, dropping to 3.2 eV for x = 1. The spectral irradiance of the Air Mass 1.5 Global Spectrum [88] is plotted in the background, which peaks at $\hbar\omega = 2.4$ eV and gradually approaches zero at around $\hbar\omega = 4.0$ eV. None of the alloy compositions exhibit a significant absorption coefficient within the visible region. The (R) values for all the alloy compositions are low, ranging between 9 % and 16 % across the energy range of interest. For comparison, the widely used solar cell material $CdSe_xTe_{1-x}$ has a much higher range of reflectivity of around (15–31)% [89]. Therefore, the combination of lower absorption coefficient and reflectivity within the visible spectrum indicates that $(In_xGa_{1-x})_2O_3$ is a promising candidate for an emitter layer in solar cell applications.

4. Conclusion

In summary, using first-principles methods, we have computationally investigated the structural, energetic, elastic, mechanical, electronic, and optical properties of $(In_xGa_{1-x})_2O_3$ alloy system in R $\overline{3}$ c crystal structure. Our results for the end members show strong agreement with available experimental and computational data. Most of our results for the intermediate members are predictive in nature because of the lack of comparable experimental results. LDOS analysis confirms the semiconducting nature of all the alloys. The formation energy and the electronic bandgap values decreased with increasing [In]. Phonon LDOS and mechanical stability calculations confirm that all the alloys are dynamically and mechanically stable. The absorption coefficient and reflectivity across the entire alloy system suggest that this material is a promising candidate as an emitter layer in solar cell applications. This work should motivate further experimental work on $(In_xGa_{1-x})_2O_3$ as a potential material for the emitter layer in solar cell technology.

CRediT authorship contribution statement

B. K C: Writing – review & editing, Writing – original draft, Visualization, Validation, Software, Methodology, Investigation. **V.T. Barone:** Writing – review & editing, Software, Methodology, Conceptualization. **S.R. Kandel:** Software, Methodology. **M. Sitaula:** Writing – review & editing, Software, Methodology. **B.B. Dumre:** Writing – review & editing. **R.J. Ellingson:** Project administration, Funding acquisition, Conceptualization. **S.V. Khare:** Writing – review & editing, Supervision, Resources, Project administration, Funding acquisition, Conceptualization.

Declaration of competing interest

The authors declare that they have no known competing financial interests or personal relationships that could have appeared to influence the work reported in this paper.

Acknowledgements

The material is based on research sponsored by the Air Force Research Laboratory (AFRL) under Agreement No. FA9453-19-C-1002. The U.S. Government is authorized to reproduce and distribute reprints for Governmental purposes, notwithstanding any copyright notation theorem. The views expressed are those of the authors and do not reflect the official guidance or position of the United States Government, the Department of Defense, or the United States Air Force. The appearance of external hyperlinks does not constitute endorsement by the United States Department of Defense (DOD) of the linked websites or the information, products, or service contained therein. The DOD does not exercise any editorial, security, or other control over the information you may find at these locations. Approved for public release; distribution is unlimited. Public Affairs approval Grant No. AFRL-2025-0687.

Computational work for this work was performed on the University of Toledo's computing clusters.

Appendix A. Supplementary data

Supplementary data to this article can be found online at https://doi.org/10.1016/j.physb.2025.417615.

Data availability

Data will be made available on request.

References

[1] J.N. Duenow, W.K. Metzger, Back-surface recombination, electron reflectors, and paths to 28% efficiency for thin-film photovoltaics: a CdTe case study, J. Appl. Phys. 125 (2019) 053101, https://doi.org/10.1063/1.5063799.
[2] T. Ablekim, E. Colegrove, W.K. Metzger, Interface engineering for 25% CdTe solar cells, ACS Appl. Energy Mater. 1 (2018) 5135–5139, https://doi.org/10.1021/acsaem.8b01173.
[3] G. Yeung, C. Reich, A. Onno, A. Bothwell, A. Danielson, Z. Holman, W.S. Sampath, C.A. Wolden, Robust passivation of CdSeTe based solar cells using reactively sputtered magnesium zinc oxide, Sol. Energy Mater. Sol. Cells 233 (2021) 111388, https://doi.org/10.1016/j.solmat.2021.111388.
[4] D.S. Ginley, C. Bright, Transparent conducting oxides, MRS Bull. 25 (2000) 15–18, https://doi.org/10.1557/mrs2000.256.
[5] O. Bierwagen, Indium oxide—a transparent, wide-band gap semiconductor for (opto) electronic applications, Semicond. Sci. Technol. 30 (2015) 024001, https://doi.org/10.1088/0268-1242/30/2/024001.
[6] J. Furthmüller, F. Bechstedt, Quasiparticle bands and spectra of Ga_2O_3 polymorphs, Phys. Rev. B 93 (2016) 115204, https://doi.org/10.1103/PhysRevB.93.115204.
[7] K. Nomura, H. Ohta, A. Takagi, T. Kamiya, M. Hirano, H. Hosono, Room-temperature fabrication of transparent flexible thin-film transistors using amorphous oxide semiconductors, nature 432 (2004) 488–492, https://doi.org/10.1038/nature03090.
[8] A. Dive, J. Varley, S. Banerjee, In_2O_3-Ga_2O_3 alloys as potential buffer layers in CdTe thin-film solar cells, Phys. Rev. Appl. 15 (2021) 034028, https://doi.org/10.1103/PhysRevApplied.15.034028.
[9] J.E. Swallow, R.G. Palgrave, P.A. Murgatroyd, A. Regoutz, M. Lorenz, A. Hassa, M. Grundmann, H. von Wenckstern, J.B. Varley, T.D. Veal, Indium gallium oxide alloys: electronic structure, optical gap, surface space charge, and chemical trends within common-cation semiconductors, ACS Appl. Mater. Interfaces 13 (2021) 2807–2819, https://doi.org/10.1021/acsami.0c16021.
[10] M. Kneiß, A. Hassa, D. Splith, C. Sturm, H. Von Wenckstern, M. Lorenz, M. Grundmann, Epitaxial stabilization of single phase κ-$(In_xGa_{1-x})_2O_3$ thin films up to x= 0.28 on c-sapphire and κ-Ga_2O_3 (001) templates by tin-assisted VCCS-PLD, APL Mater. 7 (2019) 101102, https://doi.org/10.1063/1.5120578.
[11] A. Hassa, H. Von Wenckstern, D. Splith, C. Sturm, M. Kneiß, V. Prozheeva, M. Grundmann, Structural, optical, and electrical properties of orthorhombic κ-$(In_xGa_{1-x})_2O_3$ thin films, APL Mater. 7 (2019) 022525, https://doi.org/10.1063/1.5054394.
[12] Y. Kokubun, T. Abe, S. Nakagomi, Sol–gel prepared $(Ga_{1-x}In_x)_2O_3$ thin films for solar-blind ultraviolet photodetectors, Phys. Status Solidi 207 (2010) 1741–1745, https://doi.org/10.1002/pssa.200983712.
[13] M.K. Jamarkattel, A.B. Phillips, I. Subedi, A. Abudulimu, E. Bastola, D.-B. Li, X. Mathew, Y. Yan, R.J. Ellingson, N.J. Podraza, Indium gallium oxide emitters for high-efficiency CdTe-based solar cells, ACS Appl. Energy Mater. 5 (2022) 5484–5489, https://doi.org/10.1021/acsaem.2c00153.
[14] M.K. Jamarkattel, A. Abbas, X. Mathew, S. Neupane, E. Bastola, D.-B. Li, S. Seibert, A.P. Patel, Z. Song, X. Liu, 17.2% efficient $CdSe_xTe_{1-x}$ solar cell with $(In_xGa_{1-x})_2O_3$ emitter on lightweight and flexible glass, Appl. Phys. Lett. 124 (2024) 080601, https://doi.org/10.1063/5.0193628.
[15] H. Peelaers, D. Steiauf, J.B. Varley, A. Janotti, C.G. Van de Walle, $(In_xGa_{1-x})_2O_3$ alloys for transparent electronics, Phys. Rev. B 92 (2015) 085206, https://doi.org/10.1103/PhysRevB.92.085206.
[16] X. Liu, C.-K. Tan, Electronic properties of monoclinic $(In_xGa_{1-x})_2O_3$ alloys by first-principle, AIP Adv. 9 (2019) 035318, https://doi.org/10.1063/1.5093195.
[17] H. He, R. Orlando, M.A. Blanco, R. Pandey, E. Amzallag, I. Baraille, M. Rérat, First-principles study of the structural, electronic, and optical properties of Ga_2O_3 in its monoclinic and hexagonal phases, Phys. Rev. B Condens. Matter 74 (2006) 195123, https://doi.org/10.1103/PhysRevB.74.195123.
[18] M. Grundmann, Elastic theory of pseudomorphic monoclinic and rhombohedral heterostructures, J. Appl. Phys. 124 (2018) 185302, https://doi.org/10.1063/1.5045845.
[19] J. Ding, Y. Liu, X. Gu, L. Zhang, X. Zhang, X. Chen, W. Liu, Y. Cai, S. Guo, C. Sun, Electronic transport and optical properties of five different phases (α, β, ε, δ and γ) of Ga_2O_3: a first-principles study, Phys. B Condens. Matter 682 (2024) 415888, https://doi.org/10.1016/j.physb.2024.415888.
[20] S.Z. Karazhanov, P. Ravindran, P. Vajeeston, A. Ulyashin, T. Finstad, H. Fjellvåg, Phase stability, electronic structure, and optical properties of indium oxide polytypes, Phys. Rev. B Condens. Matter 76 (2007) 075129, https://doi.org/10.1103/PhysRevB.76.075129.
[21] O. Verma, M. Meshram, A. Mishra, M.L. Verma, B.K. Rao, Structural, electronic and optical properties of In_2O_3: a density functional study, Opt. Quant. Electron. 52 (2020) 1–10, https://doi.org/10.1007/s11082-020-02347-z.
[22] T. De Boer, M. Bekheet, A. Gurlo, R. Riedel, A. Moewes, Band gap and electronic structure of cubic, rhombohedral, and orthorhombic In_2O_3 polymorphs: experiment and theory, Phys. Rev. B 93 (2016) 155205, https://doi.org/10.1103/PhysRevB.93.155205.
[23] G. Kresse, J. Furthmüller, Efficiency of ab-initio total energy calculations for metals and semiconductors using a plane-wave basis set, Comput. Mater. Sci. 6 (1996) 15–50, https://doi.org/10.1016/0927-0256(96)00008-0.
[24] G. Kresse, D. Joubert, From ultrasoft pseudopotentials to the projector augmented-wave method, Physical review b 59 (1999) 1758, https://doi.org/10.1103/PhysRevB.59.1758.
[25] N. Jiang, J.L. Roehl, S.V. Khare, D.G. Georgiev, A.H. Jayatissa, An ab initio computational study of pure Zn_3N_2 and its native point defects and dopants Cu, Ag

and Au, Thin Solid Films 564 (2014) 331–338, https://doi.org/10.1016/j.tsf.2014.05.032.
[26] J.P. Perdew, J.A. Chevary, S.H. Vosko, K.A. Jackson, M.R. Pederson, D.J. Singh, C. Fiolhais, Atoms, molecules, solids, and surfaces: applications of the generalized gradient approximation for exchange and correlation, Phys. Rev. B 46 (1992) 6671, https://doi.org/10.1103/PhysRevB.46.6671.
[27] P.E. Blochl, Projector augmented-wave method, Phys. Rev. B 50 (1994) 17953, https://doi.org/10.1103/PhysRevB.50.17953.
[28] N. Szymanski, I. Khatri, J. Amar, D. Gall, S. Khare, Unconventional superconductivity in 3d rocksalt transition metal carbides, J. Mater. Chem. C 7 (2019) 12619–12632, https://doi.org/10.1039/C9TC03793D.
[29] S. Kandel, B. Dumre, D. Gall, S. Khare, Prediction of super hardness in transition metal hexa-nitrides from density functional theory computations, Materialia 25 (2022) 101550, https://doi.org/10.1016/j.mtla.2022.101550.
[30] D.D. Le, T.S. Ngo, J.-H. Song, S.-K. Hong, Epitaxial growth of bandgap tunable $ZnSnN_2$ films on (0001) Al_2O_3 substrates by using a ZnO buffer, Cryst. Growth Des. 18 (2018) 1385–1393, https://doi.org/10.1021/acs.cgd.7b01285.
[31] D. Fang, Y. Li, Structural, electronic, and optical properties of ZnO: $ZnSnN_2$ compounds for optoelectronics and photocatalyst applications, Phys. Lett. 384 (2020) 126670, https://doi.org/10.1016/j.physleta.2020.126670.
[32] A. Jain, S.P. Ong, G. Hautier, W. Chen, W.D. Richards, S. Dacek, S. Cholia, D. Gunter, D. Skinner, G. Ceder, K.A. Persson, Commentary: the materials project: a materials genome approach to accelerating materials innovation, APL Mater. 1 (2013) 011002, https://doi.org/10.1063/1.4812323.
[33] A. Zunger, S. Wei, L.G. Ferreira, J.E. Bernard, Special quasirandom structures, Phys. Rev. Lett. 65 (1990) 353–356, https://doi.org/10.1103/PhysRevLett.65.353.
[34] A. Van De Walle, M. Asta, G. Ceder, The alloy theoretic automated toolkit: a user guide, Calphad 26 (2002) 539–553, https://doi.org/10.1016/S0364-5916(02)80006-2.
[35] I. Khare, N. Szymanski, D. Gall, R. Irving, Electronic, optical, and thermoelectric properties of sodium pnictogen chalcogenides: a first principles study, Comput. Mater. Sci. 183 (2020) 109818, https://doi.org/10.1016/j.commatsci.2020.109818.
[36] N. Szymanski, V. Adhikari, M. Willard, P. Sarin, D. Gall, S. Khare, Prediction of improved magnetization and stability in $Fe_{16}N_2$ through alloying, J. Appl. Phys. 126 (2019) 093903, https://doi.org/10.1063/1.5109571.
[37] S. Kandel, B. Dumre, D. Gall, S. Khare, Mechanical and electronic properties of transition metal hexa-nitrides in hexagonal structure from density functional theory calculations, Comput. Mater. Sci. 221 (2023) 112084, https://doi.org/10.1016/j.commatsci.2023.112084.
[38] G. Grimvall, Thermophysical Properties of Materials, Elsevier Science B.V., Amsterdam, The Netherlands, 1999.
[39] R. Hill, The elastic behaviour of a crystalline aggregate, Proc. Phys. Soc. 65 (1952) 349, https://doi.org/10.1088/0370-1298/65/5/307.
[40] A. Reuß, Berechnung der fließgrenze von mischkristallen auf grund der plastizitätsbedingung für einkristalle, ZAMM-Journal of Applied Mathematics and Mechanics/Zeitschrift für Angewandte Mathematik und Mechanik 9 (1929) 49–58, https://doi.org/10.1002/zamm.19290090104.
[41] X. Zhou, D. Gall, S.V. Khare, Mechanical properties and electronic structure of anti-ReO_3 structured cubic nitrides, M_3N, of d block transition metals M: an ab initio study, J. Alloys Compd. 595 (2014) 80–86, https://doi.org/10.1016/j.jallcom.2014.01.116.
[42] W. Voigt, Lehrbuch Der Kristallphysik:(Mit Ausschluss Der Kristalloptik), B.G. Teubner, Leipzig und Berlin, 1910.
[43] B.B. Dumre, S.V. Khare, Interrelationship of bonding strength with structural stability of ternary oxide phases of $MgSnO_3$: a first-principles study, Phys. B Condens. Matter 637 (2022) 413896, https://doi.org/10.1016/j.physb.2022.413896.
[44] P. Gunaicha, S. Gangam, J. Roehl, S. Khare, Structural, energetic and elastic properties of Cu_2ZnSn $(S_xSe_{1-x})_4$ (x= 1, 0.75, 0.5, 0.25, 0) alloys from first-principles computations, Sol. Energy 102 (2014) 276–281, https://doi.org/10.1016/j.solener.2014.01.015.
[45] S. Kandel, B. Dumre, D. Gall, S. Khare, Investigation of hardness in transition metal hexa-nitrides in cubic structure: a first-principles study, J. Phys. Chem. Solid. 171 (2022) 111022, https://doi.org/10.1016/j.jpcs.2022.111022.
[46] S. Kandel, D. Gall, S. Khare, Density functional theory calculations of mechanical and electronic properties of $W_{1-x}Ta_xN_6$, $W_{1-x}Mo_xN_6$, and $Mo_{1-x}Ta_xN_6$ ($0 \leq x \leq 1$) alloys in a hexagonal structure, J. Vac. Sci. Technol. A 41 (2023) 063112, https://doi.org/10.1116/6.0002923.
[47] K. Zhang, K. Balasubramanian, B. Ozsdolay, C. Mulligan, S. Khare, W. Zheng, D. Gall, Epitaxial NbC_xN_{1-x} (001) layers: growth, mechanical properties, and electrical resistivity, Surf. Coating. Technol. 277 (2015) 136–143, https://doi.org/10.1016/j.surfcoat.2015.07.025.
[48] M. Born, On the stability of crystal lattices. I, Math. Proc. Camb. Phil. Soc. 36 (2008) 160–172, https://doi.org/10.1017/S0305004100017138.
[49] J. Paier, M. Marsman, K. Hummer, G. Kresse, I.C. Gerber, J.G. Ángyán, Screened hybrid density functionals applied to solids, J. Chem. Phys. 124 (2006) 154709, https://doi.org/10.1063/1.2187006.
[50] J. Heyd, G.E. Scuseria, M. Ernzerhof, Hybrid functionals based on a screened Coulomb potential, J. Chem. Phys. 118 (2003) 8207–8215, https://doi.org/10.1063/1.1564060.
[51] A.V. Krukau, O.A. Vydrov, A.F. Izmaylov, G.E. Scuseria, Influence of the exchange screening parameter on the performance of screened hybrid functionals, J. Chem. Phys. 125 (2006) 224106, https://doi.org/10.1063/1.2404663.
[52] B.B. Dumre, R.J. Nelson, R.E. Irving, R.J. Ellingson, S.V. Khare, Trends in opto-electronic properties of $Mg_xZn_{1-x}SnN_2$ using first principles methods, Mater. Chem. Phys. 294 (2023) 126995, https://doi.org/10.1016/j.matchemphys.2022.126995.
[53] A.M. Ganose, A.J. Jackson, D.O. Scanlon, Sumo: command-line tools for plotting and analysis of periodic ab initio calculations, J. Open Source Softw. 3 (2018) 717, https://doi.org/10.21105/joss.00717.
[54] A. Togo, I. Tanaka, First principles phonon calculations in materials science, Scr. Mater. 108 (2015) 1–5, https://doi.org/10.1016/j.scriptamat.2015.07.021.
[55] V.L. Deringer, A.L. Tchougréeff, R. Dronskowski, Crystal orbital Hamilton population (COHP) analysis as projected from plane-wave basis sets, J. Phys. Chem. A 115 (2011) 5461–5466, https://doi.org/10.1021/jp202489s.
[56] S. Maintz, V.L. Deringer, A.L. Tchougréeff, R. Dronskowski, Analytic projection from plane-wave and PAW wavefunctions and application to chemical-bonding analysis in solids, J. Comput. Chem. 34 (2013) 2557–2567, https://doi.org/10.1002/jcc.23424.
[57] S. Maintz, V.L. Deringer, A.L. Tchougréeff, R. Dronskowski, LOBSTER: a Tool to Extract Chemical Bonding from Plane-Wave Based DFT, Wiley Online Library, 2016, pp. 1030–1035.
[58] S. Maintz, M. Esser, R. Dronskowski, Efficient rotation of local basis functions using real spherical harmonics, Acta Phys. Pol. B 47 (2016) 1165, https://doi.org/10.5506/APhysPolB.47.1165.
[59] R. Nelson, C. Ertural, J. George, V.L. Deringer, G. Hautier, R. Dronskowski, LOBSTER: local orbital projections, atomic charges, and chemical-bonding analysis from projector-augmented-wave-based density-functional theory, J. Comput. Chem. 41 (2020) 1931–1940, https://doi.org/10.1002/jcc.26353.
[60] R. Dronskowski, P.E. Blöchl, Crystal orbital Hamilton populations (COHP): energy-resolved visualization of chemical bonding in solids based on density-functional calculations, J. Phys. Chem. 97 (1993) 8617–8624, https://doi.org/10.1021/j100135a014.
[61] G. Henkelman, A. Arnaldsson, H. Jónsson, A fast and robust algorithm for Bader decomposition of charge density, Comput. Mater. Sci. 36 (2006) 354–360, https://doi.org/10.1016/j.commatsci.2005.04.010.
[62] E. Sanville, S.D. Kenny, R. Smith, G. Henkelman, Improved grid-based algorithm for Bader charge allocation, J. Comput. Chem. 28 (2007) 899–908, https://doi.org/10.1002/jcc.20575.
[63] W. Tang, E. Sanville, G. Henkelman, A grid-based Bader analysis algorithm without lattice bias, J. Phys. Condens. Matter 21 (2009) 084204, https://doi.org/10.1088/0953-8984/21/8/084204.
[64] M. Yu, D.R. Trinkle, Accurate and efficient algorithm for Bader charge integration, J. Chem. Phys. 134 (2011) 064111, https://doi.org/10.1063/1.3553716.
[65] L. Vegard, Die konstitution der mischkristalle und die raumfüllung der atome, Z. Phys. 5 (1921) 17–26, https://doi.org/10.1007/BF01349680.
[66] S. Yoshioka, H. Hayashi, A. Kuwabara, F. Oba, K. Matsunaga, I. Tanaka, Structures and energetics of Ga_2O_3 polymorphs, J. Phys. Condens. Matter 19 (2007) 346211, https://doi.org/10.1088/0953-8984/19/34/346211.
[67] F. Fuchs, F. Bechstedt, Indium-oxide polymorphs from first principles: quasiparticle electronic states, Phys. Rev. B Condens. Matter 77 (2008) 155107, https://doi.org/10.1103/PhysRevB.77.155107.
[68] M. Marezio, J. Remeika, Bond lengths in the α-Ga_2O_3 structure and the high-pressure phase of $Ga_{2-x}Fe_xO_3$, J. Chem. Phys. 46 (1967) 1862–1865, https://doi.org/10.1063/1.1840945.
[69] C.T. Prewitt, R.D. Shannon, D.B. Rogers, A.W. Sleight, C rare earth oxide-corundum transition and crystal chemistry of oxides having the corundum structure, Inorg. Chem. 8 (1969) 1985–1993, https://doi.org/10.1021/ic50079a033.
[70] K. Momma, F. Izumi, VESTA 3 for three-dimensional visualization of crystal, volumetric and morphology data, J. Appl. Crystallogr. 44 (2011) 1272–1276, https://doi.org/10.1107/S0021889811038970.
[71] M.Z. Jedrzejczyk, K, J. Rynkowski, V. Keller, J. Grams, A.M. Ruppert, N. Keller, Wide band gap Ga_2O_3 as efficient UV-C photocatalyst for gas-phase degradation applications, Environ. Sci. Pollut. Res. Int. (2017) 26792–26805, https://doi.org/10.1007/s11356-017-0253-2.
[72] D. Liu, W. Lei, S. Qin, L. Hou, Z. Liu, Q. Cui, Y. Chen, Large-scale synthesis of hexagonal corundum-type In_2O_3 by ball milling with enhanced lithium storage capabilities, J. Mater. Chem. A 1 (2013) 5274–5278, https://doi.org/10.1039/C3TA00182B.
[73] M. Born, On the stability of crystal lattices. I, Math. Proc. Camb. Phil. Soc. (1940) 160–172. Cambridge University Press.
[74] X. Liu, Y.-Y. Chang, S.N. Tkachev, C.R. Bina, S.D. Jacobsen, Elastic and mechanical softening in boron-doped diamond, Sci. Rep. 7 (2017) 42921, https://doi.org/10.1038/srep42921.
[75] S. Pugh, XCII. Relations between the elastic moduli and the plastic properties of polycrystalline pure metals, London, Edinburgh Dublin Phil. Mag. J. Sci. 45 (1954) 823–843, https://doi.org/10.1080/14786440808520496.
[76] S. Cole, M. Brown, A. Willoughby, The microhardness of $Cd_xHg_{1-x}Te$, J. Mater. Sci. 17 (1982) 2061–2066, https://doi.org/10.1007/BF00540424.
[77] T. Kawamura, T. Akiyama, Bandgap engineering of α-Ga_2O_3 by hydrostatic, uniaxial, and equibiaxial strain, Jpn. J. Appl. Phys. 61 (2022) 21005, https://doi.org/10.35848/1347-4065/ac468f.
[78] K. Matsuzaki, H. Hiramatsu, K. Nomura, H. Yanagi, T. Kamiya, M. Hirano, H. Hosono, Growth, structure and carrier transport properties of Ga_2O_3 epitaxial film examined for transparent field-effect transistor, Thin Solid Films 496 (2006) 37–41, https://doi.org/10.1016/j.tsf.2005.08.187.
[79] D. Shinohara, S. Fujita, Heteroepitaxy of corundum-structured α-Ga_2O_3 thin films on α-Al_2O_3 substrates by ultrasonic mist chemical vapor deposition, Jpn. J. Appl. Phys. 47 (2008) 7311, https://doi.org/10.1143/JJAP.47.7311.

[80] C.Y. Wang, V. Cimalla, H. Romanus, T. Kups, G. Ecke, T. Stauden, M. Ali, V. Lebedev, J. Pezoldt, O. Ambacher, Phase selective growth and properties of rhombohedral and cubic indium oxide, Appl. Phys. Lett. 89 (2006) 011904, https://doi.org/10.1063/1.2219125.

[81] A.L. Allred, E.G. Rochow, A scale of electronegativity based on electrostatic force, J. Inorg. Nucl. Chem. 5 (1958) 264–268, https://doi.org/10.1016/0022-1902(58)80003-2.

[82] B.B. Dumre, D. Gall, S.V. Khare, Stability, and electronic and optical properties of ternary nitride phases of $MgSnN_2$: a first-principles study, J. Phys. Chem. Solid. 153 (2021) 110011, https://doi.org/10.1016/j.jpcs.2021.110011.

[83] Y. Zhang, M. Liu, D. Jena, G. Khalsa, Tight-binding band structure of β-and α-phase Ga_2O_3 and Al_2O_3, J. Appl. Phys. 131 (2022) 175702, https://doi.org/10.1063/5.0074598.

[84] Y. Li, Y. Yi, V. Coropceanu, J.-L. Brédas, Optical conductivity and optical effective mass in a high-mobility organic semiconductor: implications for the nature of charge transport, Phys. Rev. B 90 (2014) 245112, https://doi.org/10.1103/PhysRevB.90.245112.

[85] S. Calnan, A. Tiwari, High mobility transparent conducting oxides for thin film solar cells, Thin Solid Films 518 (2010) 1839–1849, https://doi.org/10.1016/j.tsf.2009.09.044.

[86] P.K. Tyagi, V. Singh, N-type diamane: an effective emitter layer in crystalline silicon heterojunction solar cell, Carbon Trends 9 (2022) 100209, https://doi.org/10.1016/j.cartre.2022.100209.

[87] R. Hornreich, M. Kugler, S. Shtrikman, C. Sommers, Phonon band gaps, J. Phys. 7 (1997) 509–519, https://doi.org/10.1051/jp1:1997172.

[88] C.A. Gueymard, The sun's total and spectral irradiance for solar energy applications and solar radiation models, Sol. Energy 76 (2004) 423–453, https://doi.org/10.1016/j.solener.2003.08.039.

[89] B.B. Dumre, N.J. Szymanski, V. Adhikari, I. Khatri, D. Gall, S.V. Khare, Improved optoelectronic properties in $CdSe_xTe_{1-x}$ through controlled composition and short-range order, Sol. Energy 194 (2019) 742–750, https://doi.org/10.1016/j.solener.2019.10.091.